The Journal of Chemical Physics

Dynamics of the isotope exchange reaction of D with H_3^+, H_2D^+, and D_2H^+

Cite as: J. Chem. Phys. **154**, 084307 (2021); https://doi.org/10.1063/5.0038434
Submitted: 22 November 2020 . Accepted: 11 January 2021 . Published Online: 26 February 2021

K. P. Bowen, P.-M. Hillenbrand, J. Liévin, D. W. Savin, and X. Urbain

View Online Export Citation CrossMark

Challenge us.
What are your needs for periodic signal detection?
Watch
Zurich Instruments

© 2021 Author(s).

The Journal of Chemical Physics ARTICLE scitation.org/journal/jcp

Dynamics of the isotope exchange reaction of D with H_3^+, H_2D^+, and D_2H^+

Cite as: J. Chem. Phys. 154, 084307 (2021); doi: 10.1063/5.0038434
Submitted: 22 November 2020 • Accepted: 11 January 2021 •
Published Online: 26 February 2021

View Online Export Citation CrossMark

K. P. Bowen,[1,a] P.-M. Hillenbrand,[1,2] J. Liévin,[3,b] D. W. Savin,[1,c] and X. Urbain[4,d]

AFFILIATIONS

[1]Columbia Astrophysics Laboratory, Columbia University, New York, New York 10027, USA
[2]Institut für Kernphysik, Goethe-Universität, 60438 Frankfurt, Germany
[3]Spectroscopy, Quantum Chemistry and Atmospheric Remote Sensing (SQUARES), Université Libre de Bruxelles, B-1050 Brussels, Belgium
[4]Institute of Condensed Matter and Nanosciences, Université Catholique de Louvain, B-1348 Louvain-la-Neuve, Belgium

[a]**Electronic mail:** bowenk4@gmail.com
[b]**Electronic mail:** jlievin@ulb.ac.be
[c]**Electronic mail:** dws26@columbia.edu
[d]**Author to whom correspondence should be addressed:** xavier.urbain@uclouvain.be

ABSTRACT

We have measured the merged-beams rate coefficient for the titular isotope exchange reactions as a function of the relative collision energy in the range of ~3 meV–10 eV. The results appear to scale with the number of available sites for deuteration. We have performed extensive theoretical calculations to characterize the zero-point energy corrected reaction path. Vibrationally adiabatic minimum energy paths were obtained using a combination of unrestricted quadratic configuration interaction of single and double excitations and internally contracted multireference configuration interaction calculations. The resulting barrier height, ranging from 68 meV to 89 meV, together with the various asymptotes that may be reached in the collision, was used in a classical over-the-barrier model. All competing endoergic reaction channels were taken into account using a flux reduction factor. This model reproduces all three experimental sets quite satisfactorily. In order to generate thermal rate coefficients down to 10 K, the internal excitation energy distribution of each H_3^+ isotopologue is evaluated level by level using available line lists and accurate spectroscopic parameters. Tunneling is accounted for by a direct inclusion of the exact quantum tunneling probability in the evaluation of the cross section. We derive a thermal rate coefficient of $< 1 \times 10^{-12}$ cm^3 s^{-1} for temperatures below 44 K, 86 K, and 139 K for the reaction of D with H_3^+, H_2D^+, and D_2H^+, respectively, with tunneling effects included. The derived thermal rate coefficients exceed the ring polymer molecular dynamics prediction of Bulut *et al.* [J. Phys. Chem. A **123**, 8766 (2019)] at all temperatures.

© 2021 Author(s). All article content, except where otherwise noted, is licensed under a Creative Commons Attribution (CC BY) license (http://creativecommons.org/licenses/by/4.0/). https://doi.org/10.1063/5.0038434

I. INTRODUCTION

Bimolecular ion–molecule reactions involving H-bearing species are among the most fundamental of all gas-phase chemical processes.[1] Such reactions feature prominently in many different chemical situations, including astrochemistry,[2,3] combustion,[4,5] fusion plasmas,[6] planetary atmospheres,[7–9] and plasma processing.[10,11] Our understanding of these reactions builds on decades of benchmark laboratory measurements[12] and complementary theoretical studies.[13–16] However, experimental challenges limit the specific systems and reactions that can be studied.[17,18] Theory must be relied on to fill in the gaps; but, theoretical and computational challenges necessitate the use of approximations to make the calculations tractable.[14,19,20] To help guide the development of more reliable theoretical methods, experimental studies are needed for systems of slowly increasing complexity.

© Author(s) 2021

The simplest and most fundamental ion–molecule reactive scattering processes proceed through H_3^+, H_4^+, and H_5^+ intermediates and their isotopologues. The bulk of the related published experimental studies has focused on isotopic variants of the reaction systems,

$$H^+ + H_2, \tag{1}$$

$$H_2^+ + H_2, \tag{2}$$

$$H_3^+ + H_2. \tag{3}$$

These prototype systems have often been studied with their deuterated variants, as that enables the experimental ease of using mass spectrometry to identify the reactants and products. Brief reviews of the published experimental studies have been given by others for reaction (1),[18,21] reaction (2),[22] and reaction (3).[23–25]

Less well studied experimentally are the reactions,

$$H + H_2^+, \tag{4}$$

$$H + H_3^+, \tag{5}$$

and their isotopic variants. The dearth of laboratory studies for these two reactions has been due, in part, to the experimental challenge of generating controlled and well-quantified beams or ensembles of atomic H.[17] To the best of our knowledge, there are no published reactive scattering measurements for reaction (4); only recently have experimental results been reported by us[26] for the isotopic variant of reaction (5), namely,

$$D + H_3^+ \rightarrow H_2D^+ + H. \tag{6}$$

Here, we build on our published experimental and theoretical work[26] and present new results for

$$D + H_2D^+ \rightarrow D_2H^+ + H, \tag{7}$$

$$D + D_2H^+ \rightarrow D_3^+ + H. \tag{8}$$

The rest of this paper is organized as follows. In Sec. II, the experimental apparatus is briefly described. Section III gives an overview of the measurement and data analysis procedures. The theoretical description of the reaction paths is presented in Sec. IV. The experimental results are reported and discussed in Sec. V. A summary is given in Sec. VI.

II. EXPERIMENTAL DESCRIPTION

The experiments were performed using a dual-source, merged-fast-beams apparatus depicted in Fig. 1. With this, we can perform absolute measurements of the reaction dynamics between neutral atoms and molecular cations by measuring the number densities of the parent beams and their energies and overlap and by detecting the charged daughter products. The apparatus has been described in detail elsewhere.[26–29] Here, we provide only a brief overview, with an emphasis on those aspects that are most specific to the present results.

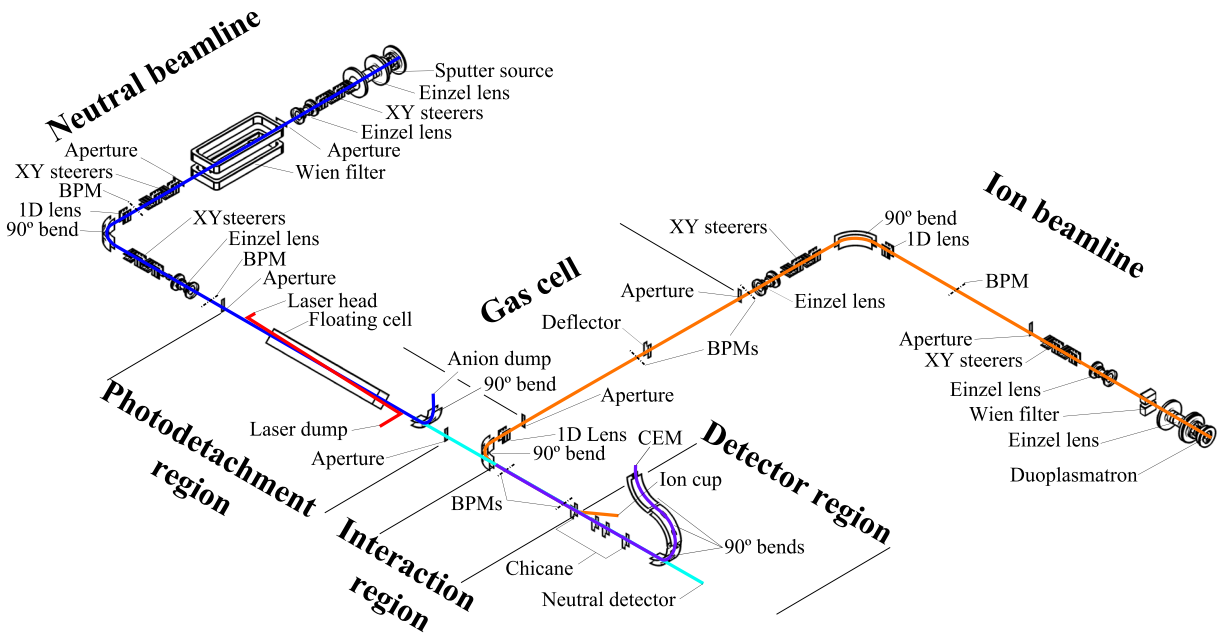

FIG. 1. Overview of the merged-beams apparatus.

© Author(s) 2021

A. Neutral D beam

We used a Peabody Scientific duoplasmatron source, operated with D_2 gas to produce D^- and floated to a voltage of V_{D^-} = −12.00 kV, −9.60 kV, and −8.00 kV for studies of reactions (6)–(8), respectively. The resulting negative particle beam was sent through a Wien filter and mass-to-charge (m/q) filtered to generate a pure beam of $D^-(^1S_0)$, as D^- has only one bound level.[30] The translational energy in the laboratory frame was $E_{D^-} = |eV_{D^-}|$, where e is the elementary charge. The beam was, then, guided using a series of electrostatic optics. Typical D^- currents after the Wien filter were 3.7 μA for reactions (6) and (7) and 3.0 μA for reaction (8). These D^- currents, and those measured further downstream, do not scale as expected with the acceleration voltage for a couple of reasons. One is that the ion optics were optimized to maximize the neutral D beam particle current in the interaction region. The second is that the filament coating in the ion source aged over the course of the measurements, which were carried out first for reaction (6), then for reaction (8), and finally for reaction (7).

The D^- beam was, then, deflected by 90° and directed into a floating cell. Typical D^- currents entering the floating cell were 3.3 μ A for reaction (6), 1.7 μA for reaction (7), and 2.5 μA for reaction (8). A voltage U_f was applied to the floating cell, resulting in an anion beam energy in the cell of $E_{D^-} + eU_f$. Within the floating cell, ground level D beams are produced via photodetachment,

$$D^-(^1S_0) + h\nu \rightarrow D(^2S_{1/2}) + e^-, \tag{9}$$

using an ~1 kW laser beam of wavelength λ = 808 nm.[31] Typically, a few percent of the anion beam is photodetached to form the desired fast neutral D beam.

The neutral beam leaves the floating cell with an energy of $E_n = E_{D^-} + eU_f$. Apertures before and after the floating cell collimate the beam. D^- remaining after the second aperture was electrostatically deflected into a beam dump. The pure ground level D beam, then, continued ballistically into the interaction region.

B. Cation beam

The H_3^+ beam was generated by introducing pure H_2 into a Peabody Scientific duoplasmatron source. Beams of H_2D^+ and D_2H^+ were produced by introducing a mixture of H_2 and D_2 gas into the duoplasmatron source in roughly equal proportion. The molecular cations are produced internally excited, with an internal temperature that is a function of source pressure. Here, the total pressure in the source was kept at p_s ~ 0.5 Torr for all measurements using an ion gauge calibrated for H_2. This enabled us to produce the molecular cations with an internal temperature of ~ 1200 K, the lowest that we could achieve with the current source configuration.[26]

The cation beam energies were chosen so as to match the neutral D beam velocity at U_f = 0 V. This resulted in $E_{H_3^+}$ = 18.02 keV for reaction (6), $E_{H_2D^+}$ = 19.21 keV for reaction (7), and $E_{D_2H^+}$ = 20.01 keV for reaction (8). The cation beam then passed through a Wien filter to select the desired beam, according to its m/q ratio. After the Wien filter, the cation beam was electrostatically deflected 90° and steered through two collimating apertures. A retractable Faraday cup after the second aperture was used to measure the ion beam current before it was merged onto the neutral beam. Typical beam currents after the second aperture were 1.1 μA for H_3^+, 1.2 μA for H_2D^+, and 0.46 μA for D_2H^+. The beam was then steered by using a cylindrical deflector onto the path of the neutral beam. The beam current after this merging deflector was monitored by using a retractable Faraday cup in the interaction region. Current measurements before and after the merging cylindrical deflector indicated that 100% of the cation beam was transmitted through the merger.

The purity of the beams used was determined in several ways. The purity of the D_2H^+ beam was 100%; since we use gases of H_2 and D_2, the only m/q = 5 ion that could be formed was D_2H^+. To determine the purity of the H_3^+ beam, we used only H_2 gas and measured the m/q = 3 and 5 currents output from the source. The lack of a measurable m/q = 5 signal indicated that there was no D contamination in the source that could produce HD^+ (m/q = 3). Hence, our m/q = 3 beam was pure H_3^+.

To determine the H_2D^+ and D_2^+ fractions in the m/q = 4 beam, we developed a novel beam diagnostic. We used the second leg of the cation beamline, between the collimating apertures, as a gas cell that was filled with an ~ 0.775 mTorr of Ar, as measured using an ion gauge calibrated for Ar. As the cation beam passed through the first half of the gas cell, a portion of the beam was neutralized, forming H_2D and D_2. Neutral H_2D is unstable and fragments,[32,33] whereas D_2 is stable. Midway between the collimating apertures, we located an electrostatic deflector with an applied voltage of 1 kV that was used to remove the cations from the beam, leaving a pure beam of neutrals. A portion of these reionized as they passed through the second half of the gas cell, forming D_2^+, H_2^+, D^+, and H^+ with laboratory translational energies of 19.21 keV, 9.62 keV, 9.62 keV, and 4.81 keV, respectively. We, then, used the beam merger as an electrostatic energy analyzer to select for and direct D_2^+ into the interaction region, where we measured the current using the retractable Faraday cup.

For a pure D_2^+ beam, ensured to be free of H_2D^+ contamination by the lack of a concurrent m/q = 5 beam, the neutralization and reionization efficiency, $r_{D_2^+}$, was determined by the ratio of the currents measured in the retractable Faraday cup with and without gas in the cell,

$$r_{D_2^+} = \frac{I^g_{D_2^+}}{I^{ng}_{D_2^+}}, \tag{10}$$

where the superscripts g and ng indicate the presence of gas or no gas in the cell, respectively. Our measurements yielded $r_{D_2^+}$ = 0.40 ± 0.02%. Here and throughout, all uncertainties are quoted at an estimated one-standard-deviation statistical accuracy.

For a m/q = 4 beam containing both H_2D^+ and D_2^+, the ratio of the currents measured in the retractable Faraday cup with and without gas in the cell can be represented as

$$r_{mix} = \frac{I^g_{m/q=4}}{I^{ng}_{m/q=4}} = \frac{I^g_{D_2^+}}{I^{ng}_{D_2^+} + I^{ng}_{H_2D^+}}. \tag{11}$$

© Author(s) 2021

Here, we have used the arguments given above to set $I^{g}_{H_2D^+} = 0$. As a result, the fraction of D_2^+ in a mixed $m/q = 4$ beam, $f_{D_2^+}$, can be determined by

$$f_{D_2^+} = \frac{r_{mix}}{r_{D_2^+}}. \quad (12)$$

Typically, $f_{D_2^+} < 3\%$. This low level of contamination results from the source parameters having been optimized for the production of triatomic cations.[26] The actual $I_{H_2D^+}$ was given by the measured current reduced by $f_{D_2^+}$.

C. Interaction region

The two beams overlap for $L = 1215$ mm, as measured from the exit of the beam merger to the entrance of an electrostatic chicane (described below). The overlap of the beams is determined using two single-wire beam profile monitors (BPMs)[34] placed near the beginning and the end of the interaction region, ~ 280 mm and 1090 mm from the exit of the merging cylindrical deflector, respectively.

The product ions for reactions (6)–(8) of H_2D^+, D_2H^+, and D_3^+, respectively, are formed at a laboratory translational energy equal to the sum of the energies of the parent beams minus the translational energy of the replaced H atom. For parent beams at matched velocities, this corresponds to a laboratory translational energy of 24.01 keV for the product ions in reactions (6)–(8).

D. Signal detection

The end of the interaction region is located within the first of four pairs of parallel plate electrodes of a chicane, which is designed to deflect the charged particles horizontally. The voltage on the first set of plates was cycled between the voltage necessary to allow the products to pass through the chicane and the voltage necessary to direct the parent cation beam into a Faraday cup, where the ion current I_i was measured. The transmission from the interaction region to this Faraday cup was 100%. The voltage applied to the rear set of plates was used to optimize the horizontal transmission of the product beam through the final analyzer.

The final analyzer consists of a series of three 90° cylindrical parallel plate deflectors, guiding the product ions along a perpendicular vertical plane. The first two deflectors, referred to as the lower cylindrical deflector (LCD) and middle cylindrical deflector (MCD), respectively, result in a 180° bend. A 5 mm slit after the exit of the MCD helps remove any parent beam that makes it into the final analyzer, a potential source of background. The third deflector, the upper cylindrical deflector (UCD), bends in the opposite direction and guides the products onto a channel electron multiplier (CEM). The transmittance from the interaction region to the exit of the UCD was measured to be $T_a = 90\% \pm 5\%$ using a proxy cation beam at the energy of the signal ions and a Faraday cup after the exit of the UCD.

The CEM counts the products with an efficiency of $\eta = 99\% \pm 3\%$.[35,36] The grid in front of the CEM has a geometric transmittance of $T_g = 90\% \pm 1\%$ and was biased negatively to prevent electrons from leaving the CEM. Voltage scans of the rear chicane, LCD, MCD, and UCD were performed to determine the range of voltages over which the product signal was essentially constant and non-zero. The voltage center of the signal plateau for each deflector was used for data collection. Our data acquisition cycle typically consisted of scanning U_f to vary E_r, which results in a different product energy for each U_f. For this reason, it was necessary to scale the chicane, LCD, MCD, and UCD voltages for each step in the data acquisition cycle, as described in detail elsewhere.[26] The measured signal rate, S, was ~ 20 s^{-1} for reactions (6) and (7) and ~ 4 s^{-1} for reaction (8).

E. Neutral current

The neutral beam travels ballistically through the interaction region, chicane, and LCD, exiting through a hole in the outer plate of the LCD and continuing into a neutral detector, referred to as the neutral cup (NC). The NC can also be reconfigured to function as a Faraday cup for ion current measurements The transmission from the interaction region to the NC, measured using proxy ion beams, was $T_n = 95\% \pm 3\%$. The total neutral current was measured by collecting the secondary emission of negatively charged particles from a metal target in the NC impacted by the neutral beam. The total neutral particle current, as measured in amperes, is given by

$$I_D = \frac{I_{NC}}{\gamma T_n}, \quad (13)$$

where I_{NC} is the secondary negative particle current measured in the neutral cup and γ is the mean number of negative particles emitted by a neutral particle striking the target. A detailed account of the procedure used for determining γ can be found elsewhere.[26] At E_D corresponding to matched beam velocities, for reaction (6), $\gamma = 1.6 \pm 0.1$, for reaction (7), $\gamma = 1.3 \pm 0.1$, and for reaction (8), $\gamma = 1.1 \pm 0.1$. Typical neutral particle currents were 43 nA, 52 nA, and 39 nA, respectively. We found that there was a small linear dependence of γ on E_D[26] and took this into account for the energy ranges studied.

III. MEASUREMENT AND ANALYSIS

Here, we provide a brief description of the signal determination and the data analysis. A more detailed discussion can be found in our previous publications.[26–28]

A. Signal determination

The signal was separated from the background by chopping both beams out of phase with one another. The laser beam for photoionization was cycled on for 5 ms and off for 5 ms in a square-wave pattern. The cation beam was electrostatically chopped with the same pattern but phase shifted by 2.5 ms. Hence, the 10 ms cycle consists of four phases. In the first phase, only the neutral beam is present, during which N_1 counts are collected. In the second phase, both beams are on, resulting in N_2 counts. The third phase consists of only the cation beam and N_3 counts. In the final phase, both beams are off, and N_4 counts are collected. The desired signal counts, N_s, are given by

$$N_s = N_2 - N_1 - N_3 + N_4. \quad (14)$$

Note that the beam-off background-only counts given by N_4 are also present in the other three chopping phases. Hence, $+N_4$ on the

© Author(s) 2021

right-hand side of Eq. (14) is to correct for the beam-off background-only contribution being added once by N_2 and subtracted twice by $-N_1-N_3$. For a given value of U_f, this cycle above is repeated for 10 s. The signal rate, S, is given by dividing N_s by the signal measurement time of $\tau = 2.5$ s within the 10 s. The statistical uncertainty in the signal is given by

$$\delta N_s = (N_2 + N_1 + N_3 + N_4)^{1/2}. \quad (15)$$

The fractional statistical uncertainty in S is given by $\delta N_s/N_s$, and the resulting uncertainty in S is $\delta S = (\delta N_S/N_S)S$.

B. Data acquisition procedure

The procedure for data acquisition remains largely unchanged from our previously published work.[26] The floating cell was scanned over three ranges for reactions (6)–(8). The scans consisted of 20 equally spaced voltages. For reaction (6), the scans were within the ranges $U_f = -0.900$ to 1.000 kV, −0.450 kV to 0.500 kV, and −0.225 kV to 0.250 kV. For reactions (7) and (8), the floating cell was scanned over $U_f = -0.720$ kV to 0.800 kV, −0.360 kV to 0.400 kV, and −0.180 kV to 0.200 kV. The voltages applied to the chicane and final analyzer were scaled synchronously with U_f. The neutral and ion current were measured before and after signal collection for each floating cell setting.

C. Relative translational energy and beam overlap

In the center-of-mass frame, the relative translational energy E_r for monoenergetic beams intersecting at an angle θ is given by[37]

$$E_r = \mu\left(\frac{E_D}{m_D} + \frac{E_i}{m_i} - 2\sqrt{\frac{E_D E_i}{m_D m_i}}\cos\theta\right), \quad (16)$$

where $m_D = 2.015$ u is the mass of D and m_i is 3.023 u for H_3^+, 4.029 u for H_2D^+, and 5.035 u for D_2H^+. The reduced mass, defined as

$$\mu = \frac{m_D m_i}{m_D + m_i}, \quad (17)$$

is 1.209 u for reaction (6), 1.343 u for reaction (7), and 1.439 u for reaction (8). The relative velocity is, then, given by

$$v_r = \sqrt{\frac{2E_r}{\mu}}. \quad (18)$$

The experimental E_r and energy spread depend on the energies and energy spreads of the beams, the divergence of the beams, and the bulk interaction angle, θ_{bulk}, between the beams. We have calculated E_r using a Monte Carlo particle ray tracing described in detail elsewhere.[27,38] These simulations incorporated the geometric constraints from the various collimating apertures in the apparatus. These constraints were adjusted slightly to reproduce the measured typical beam profiles, overlaps, θ_{bulk}, and the overlap integral $\langle\Omega(z)\rangle$. The quantities θ_{bulk} and $\langle\Omega(z)\rangle$ for reactions (6)–(8) can be found in Table I. The simulations also yield a histogram of relative translational energies throughout the interaction volume. We take the mean of this distribution as our experimental E_r and the one-standard-deviation spread of the histogram, ΔE_r, as our relative energy uncertainty.

TABLE I. Typical experimental values.

Source	Symbol	Value for reaction (6)	Value for reaction (7)	Value for reaction (8)	Uncertainty (%)	Units
Non-constants						
Signal rate (statistical)	S	20	20	4	< 10%	s^{-1}
D velocity	v_D	10.7	9.6	8.8	≪ 1	10^7 cm s^{-1}
D current	I_D	43	52	39	5	nA
Ion current	I_i	1.1	1.2	0.46	5	μA
Bulk angle	θ_{bulk}	0.39 ± 0.19	0.69 ± 0.18	0.69 ± 0.28		mrad
Overlap factor	$\langle\Omega(z)\rangle$	2.8	3.1	3.4	10	cm^{-2}
Neutral detector efficiency	γ	1.6	1.3	1.1	6	
Constants						
Ion velocity	v_i	10.7	9.6	8.8	≪ 1	10^7 cm s^{-1}
Analyzer transmission	T_a	0.90	0.90	0.90	5	
Grid transmission	T_g	0.90	0.90	0.90	1	
Neutral transmission	T_n	0.95	0.95	0.95	3	
CEM efficiency	η	0.99	0.99	0.99	3	
Interaction length	L	121.5	121.5	121.5	2	cm
Total systematic uncertainty					15	

© Author(s) 2021

Additional fine tuning of calculated E_r was performed by comparing the data acquired at positive and negative U_f. The measurements are expected to be symmetric around $v_r = 0$ (i.e., $E_r = 0$). A small correction to the D^- source energy of < -10 V was applied in order to produce the expected symmetry. This small correction is attributed to slight differences in the plasma potentials between the duoplasmatron sources. Taking this into account, as well as the ±10 eV energy spread of each source, the minimum experimental E_r was 9 ± 7 meV for reactions (6) and (7) and 10 ± 7 meV for reaction (8). These correspond to translational temperatures of ≈ 70 K and ≈ 80 K, respectively.

D. Merged-beams rate coefficient

We measure a merged-beams rate coefficient, which is the reaction cross section σ, times the relative velocity between the colliding particles, convolved with the energy spread of the experiment. In terms of measurable quantities, the merged-beams rate coefficient and corresponding uncertainty for a given U_f scan i and voltage step j within the scan is given by

$$\langle \sigma v_r \rangle_{i,j} = (S_{i,j} \pm \delta S_{i,j}) \frac{1}{T_a T_g \eta} \frac{e^2 v_D v_i}{I_D I_i} \frac{1}{L \langle \Omega(z) \rangle}, \tag{19}$$

where v_D is the D beam velocity and v_i is the ion beam velocity. Typical values for each parameter for reactions (6)–(8) are given in Table I. The quantities that may vary during the course of a scan are listed under *non-constants*, and those that do not vary are listed under *constants*. We measure each of the quantities on the right-hand side of Eq. (19), enabling us to generate absolute results, independent of any normalization.

To determine $\langle \sigma v_r \rangle_j$ from a series of U_f scans, referred to as a data run, we used the unweighted average of the results from all voltage scans i,

$$\langle \sigma v_r \rangle_j = \frac{\sum_{i=1}^{i_{max}} \langle \sigma v_r \rangle_{i,j}}{i_{max}}. \tag{20}$$

Data runs were combined by taking the statistically weighted average of all $\langle \sigma v_r \rangle_j$ measured at the same U_f. More details can be found in our previous publication.[26]

IV. THEORETICAL CONSIDERATIONS

In this section, we first develop a series of general prescriptions that apply to the isotope exchange reactions studied here. We, then, present an *ab initio* characterization of the energy profiles for the four pathways available for isotope exchange. Finally, the calculated profiles are used to determine the transmission probabilities across the effective barrier of the reaction.

A. Characterization of the reaction path

The molecular rearrangements occurring along the reaction path of the isotope exchange reactions (6)–(8) are illustrated schematically in Fig. 2. The collisions of a D atom with H_3^+ and its mono- and bi-deuterated isotopologues are described by pathways (a), (b) + (c), and (d), respectively. They follow a pathway detailed in previous *ab initio* investigations of the Born–Oppenheimer (BO)

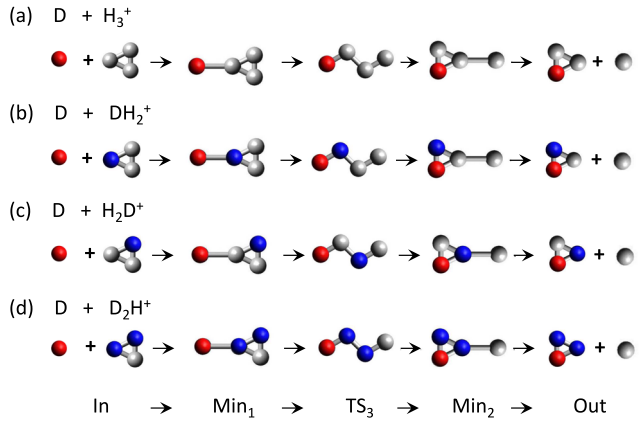

FIG. 2. Molecular rearrangements along the reaction paths for the exchange reactions involving the collision of a deuterium atom (colored in red) with H_3^+ and its mono- and bi-deuterated isotopologues. The D atoms in the initial H_3^+ isotopologues are colored in blue. Paths (b) and (c) differ by the initial orientation of the mono-deuterated H_3^+ species (see the text).

potential energy surface (PES) of H_4^+, which is the intermediate of the reactions under study.[26,39–41] After the initial collision, the system stabilizes in a first minimum Min_1, crosses the potential energy barrier characterized by transition state TS_3, and reaches a second minimum Min_2 before dissociating into the reaction products. The nomenclature of the stationary points of the PES is adopted from previous works.

The successive steps of the paths depicted in Fig. 2 can be written in a general way as

$$\begin{aligned} D + [XYZ]^+ &\rightarrow \{D\text{-}[XYZ]\}^+ \rightarrow \{D\text{-}X\text{-}Y\text{-}Z\}^+ \\ &\rightarrow \{[DXY]\text{-}Z\}^+ \rightarrow [DXY]^+ + Z, \end{aligned} \tag{21}$$

$$\begin{aligned} D + [XYZ]^+ &\rightarrow \{D\text{-}[XYZ]\}^+ \rightarrow \{D\text{-}X\text{-}Z\text{-}Y\}^+ \\ &\rightarrow \{[DXZ]\text{-}Y\}^+ \rightarrow [DXZ]^+ + Y, \end{aligned} \tag{22}$$

where X, Y, and Z are H or D atoms, with X denoting the atom of the H_3^+ isotopologue pointing in the direction of the colliding D atom. [XYZ] symbolizes a three-atom cycle, and the curly brackets indicate the range of delocalization of the positive charge. Two different paths result from a given initial orientation of the reactants. These paths are common up to Min_1, after which they bifurcate to form two different transition states, $\{D\text{-}X\text{-}Y\text{-}Z\}^+$ and $\{D\text{-}X\text{-}Z\text{-}Y\}^+$, depending on whether it is the XZ or XY bond of the Min_1 cycle that is broken, respectively. Both paths, then, follow their own route to the exit channel, releasing Z and Y as the atomic fragment, respectively. It must be stressed that the isotopic exchange takes place only if Z is an H atom in the case of path (21) or if Y is an H atom in path (22). Only paths obeying these conditions are retained for the interpretation of our experimental results.

Another point to be considered is that the H_3^+ species can orient itself toward the D atom as the reactants approach one another. Three orientations are possible, each of which can lead to pathway (21) or (22). This brings to six the number of potentially open

© Author(s) 2021

routes, each with an equal probability for a reaction to occur. Permutational symmetry of identical atoms must, however, be used to identify the symmetry equivalent paths. Each path can, then, be characterized by its multiplicity, defined as the number of symmetry equivalences. Multiplicities enable the prediction of relative probabilities.

Application of the above prescriptions to the different reactions leads to the following predictions:

- D + H_3^+ reaction: in this reaction, X, Y, and Z are identical hydrogen atoms. Stationary points have symmetry equivalent structures whatever the initial orientation, and all paths are symmetry equivalent, isoenergetic, and equiprobable. This reaction is described by path (a) of Fig. 2 and has a multiplicity of 6.
- D + mono-deuterated H_3^+ reaction: in this case, two independent collisions must be considered, D + DH_2^+ and D + H_2D^+, depending on if X = D or H, respectively. When X = D, reactions (21) and (22) exhibit the same $\{D\text{-}D\text{-}H\text{-}H\}^+$ transition state structure, give rise to the D/H exchange, and are symmetry equivalent. This path of multiplicity 2 is represented by path (b) of Fig. 2. When X = H, the transition states formed in reactions (21) and (22) are $\{D\text{-}H\text{-}D\text{-}H\}^+$ and $\{D\text{-}H\text{-}H\text{-}D\}^+$, respectively. These reactions produce, respectively, atomic H and D at dissociation and are both of multiplicity 2, but only the former contributes, as path (c) of Fig. 2, to the isotopic exchange.
- D + bi-deuterated H_3^+ reaction: this reaction also involves two different initial orientations. When X = D, two TS_3 structures $\{D\text{-}D\text{-}D\text{-}H\}^+$ and $\{D\text{-}D\text{-}H\text{-}D\}^+$ are formed, of which only the first arrangement leads to isotopic exchange. This path of multiplicity 2, given the number of possible D permutations, corresponds to path (d) of Fig. 2. No exchange is, however, possible when X = H because Y and Z are both D atoms.

In conclusion, we have identified four pathways (a)–(d), which describe the exchange reactions experimentally observed. Their multiplicities of 6, 2, 2, and 2, respectively, lead to a probability ratio of 3:2:1 for reactions (6)–(8), respectively, and a ratio of 1:1 for the two pathways characterizing reaction (7).

B. *Ab initio* methods of calculation

Two complementary sets of calculations were carried out to characterize the energy profile of the reaction paths depicted in Subsection IV A. The first, presented in Sec. IV C, focuses on the characteristic points occurring along the paths (stationary points, and entrance and exit channels) and provides accurate zero-point energy (ZPE)-corrected energies at these points. The second, presented in Sec. IV D, aims at determining the minimum energy path passing through these characteristic points and at calculating the ZPE-corrected energy curves as a function of the reaction coordinate, providing a realistic numerical description of the barrier shape, which we can, then, use in tunneling calculations (see Sec. IV E).

Specific *ab initio* approaches were adopted for both sets of calculations. The first calculations were carried out with the Molpro program package,[42,43] using the internally contracted multireference configuration interaction (ic-MRCI) method,[44,45] with an active space of 16 molecular orbitals and the extended aug-cc-pV5Z basis set.[46,47] Geometry optimization and harmonic vibrational ZPE calculations were performed at this level of theory, similar to our previous work, to which we refer the reader for more details.[26] ZPE-corrected energies E_{cor} were obtained by adding the ZPE corrections to the corresponding BO energies E_{BO},

$$E_{cor} = E_{BO} + \text{ZPE}. \tag{23}$$

We note that although no significant multi-reference character occurs in the wave functions, it is, nevertheless, worthwhile to adopt an MRCI approach for extending the configuration basis set beyond the single and double excitations scheme and obtain in this way reliable reference results, which are close to the full-configuration-interaction limit.

The second set of calculations was carried out with the Gaussian 16 program package,[48] in which specific methods for determining reaction paths are available. The minimum energy paths were calculated by means of a second order reaction-path-following approach[49,50] using the Intrinsic Reaction Coordinate (IRC).[51] Frequencies of the vibrations perpendicular to the reaction path, referred to as the projected frequencies,[52,53] were, then, calculated at each point of the IRC by projecting out of the Hessian matrix the motion in the direction of the path.[54] ZPE corrections related to these projected frequencies will be referred to below as ZPE_p to differentiate them from those arising from unprojected calculations, such as those performed in the first set of calculations. Adding ZPE_p corrections to the BO energies along the IRC provides the so-called vibrationally adiabatic (VA) energy curves.

The level of *ab initio* theory adopted for the second set of calculations has been selected to be compatible with the IRC algorithms in Gaussian 16. As the ic-MRCI method is not implemented in that program, we have instead used the unrestricted quadratic configuration interaction of single and double excitations (UQCISD) method[55] and the cc-pVQZ basis set.[46] This level of theory is, however, somewhat less accurate than our reference ic-MRCI calculations mainly in the evaluation of the relative energies characterizing the energy profiles. This is due to the lack of completeness of the one- and multiple-electron basis sets in the UQCISD calculations. The latter level is, however, good enough to determine the IRCs of the reactions. Test calculations indeed show that geometrical parameters optimized at the stationary points using both approaches agree to within better than 0.2%. A similar conclusion holds for the calculation of ZPE values, which agree to within better than 0.4%. As only the energies are affected by the change in the method, this allowed us to exploit the advantages of both approaches by recalculating at the ic-MRCI/aug-cc-pV5Z level the BO energy at the geometries along the UQCISD paths and by correcting these energies by the UQCISD ZPE_p values. We show below that the relative energies resulting from this hybrid procedure agree to within 1 meV with the full ic-MRCI results.

C. Stationary point calculations

The ZPE-corrected energies E_{cor} of the characteristic points along the pathways of Fig. 2 are reported in Table II. The results have all been obtained using the ic-MRCI/aug-cc-pV5Z level of

© Author(s) 2021

TABLE II. ZPE-corrected energy differences characterizing pathways (a)–(d) of Fig. 2, calculated at the ic-MRCI/aug-cc-pV5Z level of theory and given with respect to the corresponding entrance channel energy. The potential wells, barrier height, and reaction energies (all given in meV) correspond, respectively, to the energies of the minima Min_1 and Min_2, transition state TS_3, and exit channel. For each pathway, the first line gives the ZPE-corrected energies (E_{cor}), while the second gives in parentheses the corresponding ZPE corrections. [a]

Pathway	Potential wells		Barrier height E_b	Reaction energy. ΔE
	Min_1	Min_2	TS_3	
(a) $D + H_3^+$ [b]	−204.66	−245.74	67.98	−58.20
	(39.32)	(−1.76)	(−76.01)	(−58.20)
(b) $D + DH_2^+$	−198.34	−245.51	80.35	−54.33
	(45.64)	(−1.53)	(−63.64)	(−54.33)
(c) $D + H_2D^+$	−200.03	−241.54	82.90	−54.33
	(43.95)	(2.43)	(−61.10)	(−54.33)
(d) $D + D_2H^+$	−200.22	−247.32	89.14	−54.37
	(43.75)	(−3.34)	(−54.85)	(−54.37)

[a]According to (23), $E_{BO} = E_{cor} - ZPE$, with identical values for all isotopologues, i.e., −243.98 meV for Min_1 and Min_2, 143.99 meV for TS_3, and 0.0 meV for ΔE, as already reported by Hillenbrand *et al.*[26]
[b]The rotational ZPE of H_3^+ has been used for calculating all energies for this path (see the text for details).

theory. The energies are given with the entrance channel energy subtracted out. The table entries provide the depth of potential wells Min_1 and Min_2, the barrier height E_b of TS_3, and the reaction energy ΔE. According to our energy convention, energies below the entrance channel are negative, which means that all reactions are exoergic. The absolute value of ΔE, thus, provides the corresponding exoergicities of these reactions. The ZPE corrections to the characteristic energies, which differentiate the four paths, are given in parentheses in Table II. The variations between the different ZPE corrections at a given characteristic point show the importance of the isotopic effect (neglected within the BO approximation), in particular, for the barrier heights and the reaction energies. The latter values are equal to the ZPE differences between the isotopologues of H_3^+ involved in the entrance and exit channels.

The absolute BO energy values used for calculating the energy differences reported in Table II can be found in our previous work.[26] The harmonic ZPE values are given in Table III. The variations of the harmonic ZPE values from one isotopologue to another depend, as explained previously,[26] on the relative positions of the D atoms in the molecular structure, i.e., they are a nuclear mass effect.

For the case of H_3^+, it follows from the Pauli principle applied to the three equivalent fermionic H nuclei of this system of D_{3h} symmetry that the ground rotational level $J = K = 0$ (with J being the rotational angular momentum and K being its projection along the C_3 symmetry axis) is forbidden.[56] The rotational excitation of the lowest allowed level $J = K = 1$ of 64.12 cm^{-1} (8 meV) is, thus, to be added to the ground state ZPE to form the so-called rotational ZPE of H_3^+.[56–58] For the case of the three bosonic D nuclei of D_3^+, also of D_{3h} symmetry, the ground rovibrational state is Pauli allowed.

The E_b values of Table II are to be compared to those of the recent work of Bulut *et al.*,[59] which report values of 87 meV, 108 meV, 108 meV, and 99 meV for paths (a)–(d), respectively. Note that no difference was made in their work between paths (b) and (c) for the mono-deuterated reaction. Their values, from their work on H_4^+ BO-PES[41] and obtained at the same level of *ab initio* theory as ours, differ significantly from our values of 68 meV, 80 meV, 83 meV, and 89 meV, respectively. These discrepancies arise from several different sources. First, there is a systematic error of 6 meV in their evaluation of the E_b values, which appears when applying expression (23) using the data reported in Table I of Bulut *et al.*[59] Another difference of 8 meV appears in the case of path (a) because they did not account for the rotational contribution to the ZPE of H_3^+. Finally, discrepancies of 1.5 meV–4.5 meV are observed in the ZPE contributions to the barrier heights. Such differences are larger than the uncertainties of the corresponding harmonic frequency calculations used. For example, for the reaction of $H + H_3^+$, we compared[26] our ZPE value of TS_3 of 4167 cm^{-1} to that calculated by Sanz-Sanz *et al.*[41] and found agreement to within 0.1 cm^{-1}, while Bulut *et al.*[59] reported a value of 4202 cm^{-1}, probably obtained indirectly from the analytical expression of the PES.

The results presented in this section show that the height of the ZPE-corrected barrier E_b increases with the number n of D atoms in the $H_{3-n}D_n^+$ isotopologue: 68 meV, 80/83 meV, and 89 meV for $n = 0, 1$, and 2, respectively. This increase comes from the ZPE contribution to E_b (−76 meV, −64/−61 meV, and −55 meV, respectively), which is the difference between the ZPE of TS_3 and the ZPE of the H_3^+ isotopologue in the

TABLE III. Harmonic ZPE values characterizing pathways (a)–(d) of Fig. 2, calculated at the ic-MRCI/aug-cc-pV5Z level of theory. The imaginary frequencies ω_i of TS_3 are given in parentheses. All values are given in cm^{-1}.

Pathway			In	Min_1	Min_2	TS_3	Out
(a) $D + H_3^+$	→	$DH_2^+ + H$	4555.7[a]	4872.7	4541.8	3942.5 (875.9)	4086.3
			4491.5[b]				
(b) $D + DH_2^+$	→	$D_2H^+ + H$	4086.3	4454.4	4074.0	3573.0 (788.1)	3648.1
(c) $D + H_2D^+$	→	$D_2H^+ + H$	4086.3	4440.8	4105.9	3593.5 (789.0)	3648.1
(d) $D + D_2H^+$	→	$D_3^+ + H$	3648.1	4001.0	3621.1	3205.7 (736.4)	3177.2

[a]Rotational ZPE of H_3^+ used in Table II (see the text).
[b]ZPE of the forbidden rovibrational ground state of H_3^+.

© Author(s) 2021

entrance channel. The observed trend is explained by the more rapid decrease in ZPE with increasing n for the case of the strongly linked H_3^+ species than for the weakly bound transition state. The fact that the barrier height increases more significantly with the first increment in n than for the second one results from the 8 meV rotational contribution to the ZPE of H_3^+. Ignoring this contribution to focus on the vibrational effects only would increase the barrier height of reaction D + H_3^+ to 76 meV, leading, then, to an almost linear variation of E_b with n.

The imaginary frequencies ω_i characterizing the transition state TS_3 are also reported for each pathway, in parentheses in Table III. These frequencies characterize the negative curvature of the BO potential at the top of the reaction barrier and are usually related to the corresponding barrier width. They form, with the values of the barrier heights, the basic set of parameters used for estimating the tunneling probabilities by means of simple one-dimensional (1D) analytical forms of the barrier, such as Eckart barriers.[60,61] These approaches only provide, however, a crude approximation of the reaction energy profile. They do not take into account the change in curvature due to the ZPE corrections nor the evolution of the curvature along the path. They ignore also the existence of intermediate minima, such as can be seen in the reactions under study.

D. Vibrationally adiabatic minimum energy paths (ZPE$_p$ corrected)

We present in this subsection the second set of calculations, which have been carried out with the Gaussian 16 program in the framework of the vibrationally adiabatic (VA) approximation. Using these calculations, we aim at obtaining more realistic energy profiles, in which a ZPE_p correction is included at all points of the paths. The VA approximation, initially introduced by Marcus,[62] has been widely used, namely, in the framework of variational transition state theory[53] and reaction-path Hamiltonian methods.[52] It assumes that the motion along the reaction coordinate is separable from the other motions of the colliding system and that these other motions adjust adiabatically to the former. The resulting VA effective potential E_{VA} can, then, be used in a quantum mechanical treatment of the tunneling.[63] A common way to implement this approach by means of *ab initio* techniques is to calculate the IRC, which is the path of steepest descent in mass-weighted Cartesian coordinates beginning in the direction of the negative curvature away from the transition state and following the gradient of the PES in the direction of the reactants and of the products. The IRC provides the BO potential energy E_{BO} as a function of the reaction coordinate s, defined as the arc length along the path. For an N-atom non-linear molecule, $3N$-7 vibrations are orthogonal to the path direction at each point of the reaction coordinate. These frequencies are the so-called projected frequencies, and resulting ZPE_p is given by their sum divided by 2. This value can be added to the BO energy to furnish the energy E_{VA} at the point considered,

$$E_{VA}(s) = E_{BO}(s) + ZPE_p(s). \quad (24)$$

We have calculated the IRC paths and projected frequencies for pathways (a)–(d). For completeness, the calculations were also performed for the reference reaction H + H_3^+ → H_3^+ + H. The calculated $E_{VA}(s)$ and $ZPE_p(s)$ curves are shown in Figs. 3 and 4, respectively, in

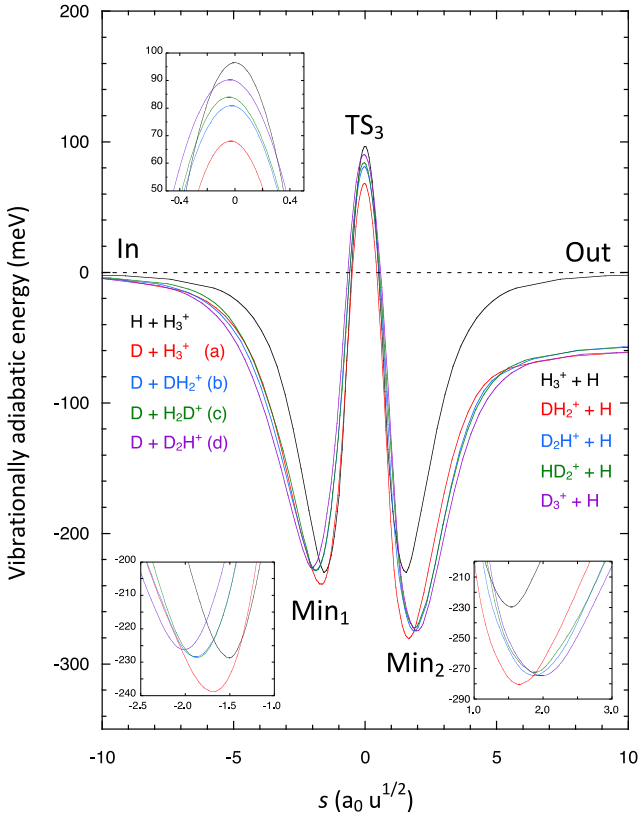

FIG. 3. Vibrationally adiabatic E_{VA} energy curves of paths (a)–(d) of Fig. 2. The curve of the reference reaction H + H_3^+ is also provided for completeness. The insets show the detailed behavior of E_{VA} around Min_1, TS_3, and Min_2.

which the corresponding entrance channel energies have been subtracted out. The mass-weighted reaction coordinate is expressed in the units of a_0 $u^{1/2}$, where a_0 is the atomic unit of length and u is the atomic mass unit. The VA curves shown in Fig. 3 are tabulated in Tables SI–SV of the supplementary material.

The VA calculations were made by applying the following computational steps to calculate each path. The central part of the profile has been first calculated. Starting from TS_3 as the initial geometry, the path was followed in both directions to Min_1 and Min_2. The entrance and exit channels were, then, calculated starting from a geometry where the fragments were fixed at a large distance from each other, and the other internal parameters were optimized. An IRC path was followed from this point in the direction of the descending gradient until Min_1 or Min_2 was reached. Additional points were calculated in the vicinity of the minima to improve the description of the potential wells. These various curves were, then, combined to provide the $E_{BO}(s)$ curve at the UQCISD/cc-pVQZ level of theory. The total number of calculated points per path is of about 110. The projected frequencies and the corresponding $ZPE_p(s)$ values were calculated at all points. The $E_{BO}(s)$ curve was, then, recalculated at the ic-MRCI/aug-cc-pV5Z level of theory using the Molpro program. The final $E_{VA}(s)$ curves were obtained by using in Eq. (24) the E_{BO}(s)/ic-MRCI and $ZPE_p(s)$/UQCISD values. For

© Author(s) 2021

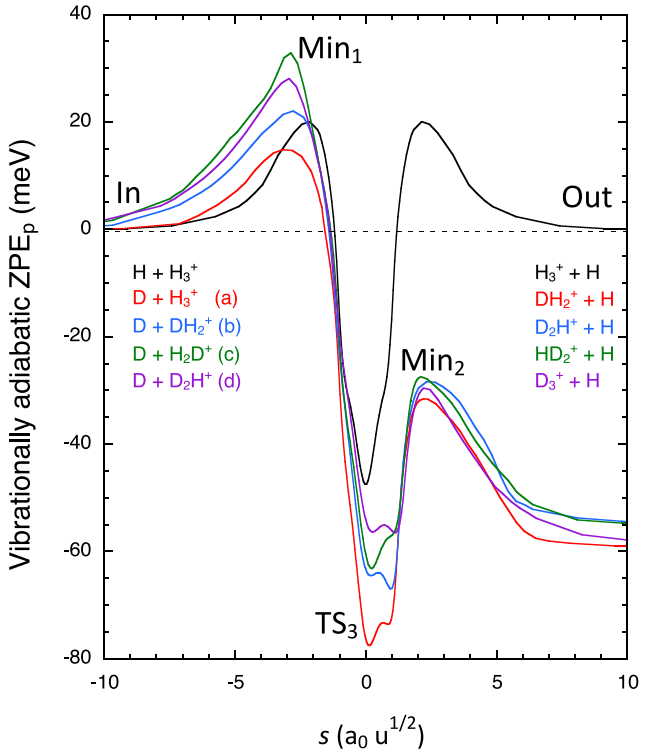

FIG. 4. Vibrationally adiabatic ZPE_p curves corresponding to the energy curves of Fig. 3.

the case of H or D + H_3^+, an analytical correction has been applied to the entrance channel to ensure the convergence to the rotational ZPE at large negative s values.

The energies of the stationary points of the E_{VA} curves can be compared with our reference values reported in Table II as a consistency check. The barrier heights and reaction energies agree to within less than 1 meV, confirming the accuracy of the procedure used for obtaining the VA energies. Larger differences are, however, observed for the depths of the potential wells, which are overestimated by the VA approximation by 26 meV–35 meV, depending on the isotopologue and the minimum considered (Min_1 or Min_2). These differences are inherent to the VA approximation, for which only the vibrations transverse to the reaction path are taken into account in the ZPE_p calculation. The vibration in the direction of the path is, thus, excluded from this correction. The contribution to the ZPE of the vibrational frequency along the path ranges from 210 cm^{-1} to 280 cm^{-1} at the equilibrium position of the minima, which corresponds to the energy differences discussed above. Only the part of the path located around the minima is affected by this contribution. This frequency is imaginary along the descent from TS_3 to the minima and from the dissociation channels to the minima and is, therefore, not taken into account in the calculation of the unprojected ZPE. The quantum mechanical motion along the reaction coordinate will be explicitly treated in the tunneling factor calculations presented in Sec. IV E.

Figures 2 and 3 clearly show the specificities of the different pathways, in particular, in the region of the three stationary points for which enlarged views are provided in corresponding insets of Fig. 3. The comparison with the symmetrical H + H_3^+ reaction shows the asymmetry induced by deuteration whose effects are detailed in Fig. 4 for VA ZPE_p. The difference between the positive and negative ranges of s shown in Fig. 3 is important, with a larger stability of Min_2 with respect to Min_1 and with the exoergicity, as already pointed out in our analysis of Table II. The slope of the asymmetric E_{VA} curves is found to be steeper on the Min_2 side of the barrier than on the Min_1 side, and a displacement of the extrema along the s axis is also observed in the insets.

The evolution of the projected frequencies and of the related ZPE_p value along the path is shown illustratively in Fig. 5 for the case of the D + H_3^+ reaction. The vibrational modes are numbered by decreasing frequency order at the geometry of the global minimum Min_1. The evolution of the related normal coordinates is

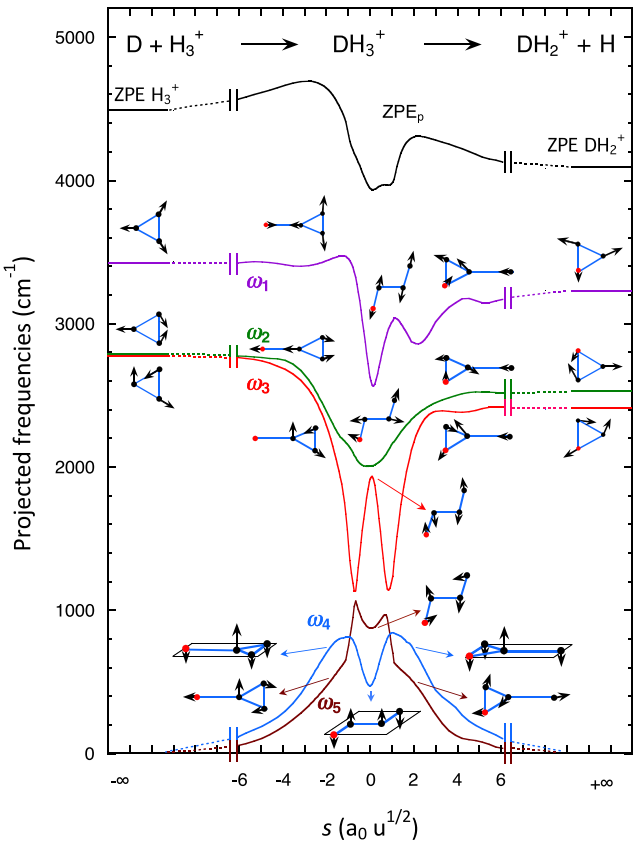

FIG. 5. Evolution of the projected frequencies and ZPE_p along reaction path (a) of reaction D + H_3^+. The rotational contribution to the ZPE of H_3^+ is not taken into account. Sketches of the normal coordinates are drawn along each frequency curve. They depict the vibrational motion at characteristic points located at $s = -\infty$, −1.9, 0, 1.9, and $+\infty$, corresponding to H_3^+, Min_1, TS_3, Min_2, and DH_2^+, respectively. H and D atoms are marked by the black and red balls, respectively.

© Author(s) 2021

illustrated by the sketches in Fig. 5 drawn at the characteristic points of the path corresponding to H_3^+, Min_1, TS_3, Min_2, and DH_2^+. These drawings show that all modes correspond to in-plane vibrations, except ω_4. The ω_1 vibration frequency corresponds to a ring breathing, ω_2 and ω_3 to ring deformations, ω_4 to an out-of-plane ring bending, and ω_5 to an in-plane ring reorientation. It can also be seen that vibrations ω_1, ω_2, and ω_3 of DH_3^+ correlate adiabatically with the vibrations of H_3^+ and DH_2^+ when s tends to $-\infty$ and $+\infty$, respectively, noting the degeneracy of ω_2 and ω_3 for H_3^+. We also note that at both dissociation limits, the frequencies ω_4 and ω_5, which involve the relative motions of the two fragments, go to 0. Figure 5 also gives some insight into the quantum mechanical information embedded in the VA model. It shows that the ZPE_p curve results from half the sum of the five frequency profiles, which show significant variations as a function of s, due to the quantum interactions governing the vibrational degrees of freedom. In particular, the existence of avoided crossings between vibrations ω_3 and ω_5 of the same a′ symmetry of DH_3^+ is responsible for the peaks observed in their profile on both sides of the barrier and for corresponding inflections in the ZPE_p curve.

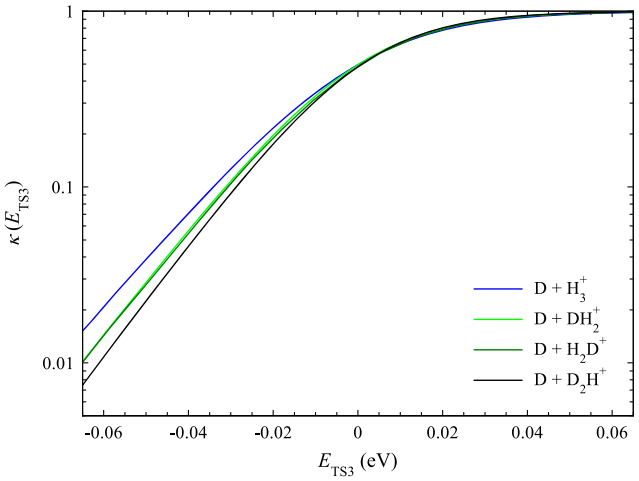

FIG. 6. Quantum tunneling probability κ as a function of the total energy available relative to the ZPE of the transition state, E_{TS3}. The curves for D + DH_2^+ and D + H_2D^+ lie nearly on top of one another.

E. Tunneling

The complete knowledge of the ZPE-corrected energy curves for all isotopic reactions allows us to go beyond the approximate Eckart potential formulas that we introduced in our preceding work[26] in order to evaluate the tunneling factor $\Gamma(T)$ to apply to the classical thermal rate coefficient. In brief, one must compute the ratio of the transmitted to the incident flux, which defines the permeability of the barrier,

$$\kappa = \frac{k_{out}}{k_{in}} \left| \frac{A_T}{A_I} \right|^2, \tag{25}$$

where k_{in} and k_{out} are the asymptotic momenta in the reactant and product channels, respectively, and A_I and A_T are the incident and transmitted amplitudes, respectively.

Here, we closely follow the prescription of Le Roy *et al.*,[64] which boils down to solving a 1D Schrödinger equation along the reaction coordinate s, with the help of a renormalized Numerov algorithm. While it is difficult to perform such a forward calculation in a time-independent manner due to the presence of some reflected amplitude, it is straightforward to consider instead the problem from the product side, where the outgoing wave is well defined. The real and imaginary part of the wavefunction $\Psi(s)$ are propagated backward from $s = +\infty$ by imposing asymptotic cosine and sine behavior at $s \to +\infty$ of

$$\phi_1(s) = A_T \cos(k_{out} s), \tag{26}$$

$$\phi_2(s) = A_T \sin(k_{out} s). \tag{27}$$

After backward propagation, the real wave functions ϕ_1 and ϕ_2 are compared to the real and imaginary parts of the wavefunction on the reactant side ($s \to -\infty$),

$$\Psi(s) = A_I \exp(ik_{in} s) + A_R \exp(-ik_{in} s), \tag{28}$$

where A_R is the reflected amplitude. The various amplitudes are retrieved by equating the log-derivative of the propagated and asymptotic wave functions at $s \to -\infty$.

The permeability κ was computed for the various reaction energy profiles (Fig. 3) by applying this algorithm in mass-weighted reaction coordinates. The result is presented in Fig. 6 as a function of the total energy available above the ZPE-corrected transition state, E_{TS3}, for the various systems. The combined effect of the reduced mass and the barrier height causes this tunneling probability to be more strongly suppressed for more deuterated systems. Note the incomplete transmission across the barrier in the immediate vicinity of $E_{TS3} = 0$. This is an example of how a submerged barrier may affect the overall reactivity.[65]

V. RESULTS AND DISCUSSION

A. Experimental merged-beams rate coefficient

Our measured $\langle \sigma v_r \rangle$ vs E_r for reactions (6)–(8) are shown in Fig. 7. The results are shown for $E_r \approx 0.01 - 10$ eV. The data plotted for reaction (6) have been published earlier.[26] The data for reactions (7) and (8) are given in Tables SVI and SVII of the supplementary material, respectively. The data points are plotted in Fig. 7 with the one-standard-deviation error bars for both $\langle \sigma v_r \rangle$ and E_r. The solid curves are from fits to the data points that have been generated using the model introduced in our previous publication[26] and adjusted to reflect the differing number of D substitution channels available for reactions (6)–(8). Further details on the model are discussed below.

B. Competing channels

For reactions (6)–(8), all competing reaction channels are endoergic. Our measurements span the thresholds for these

© Author(s) 2021

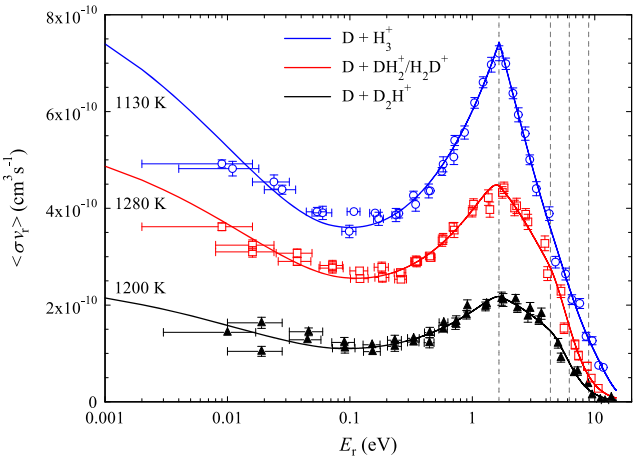

FIG. 7. Merged-beams rate coefficient $\langle \sigma v_r \rangle$ vs relative translational energy E_r for reactions (6)–(8), shown in blue, red, and black, respectively. The different symbols represent the experimental data. The vertical error bars represent the one-standard-deviation statistical uncertainty, and the horizontal error bars show the one-standard-deviation energy spread at each E_r. The various curves show the fits to these points, generated using the model described in Sec. V C, for molecular cations with an internal temperature of ~ 1200 K (solid lines). The corresponding best fit temperatures are given above each curve. The vertical dashed lines indicate the appearance threshold of the competing fragmentation channels, as listed in Sec. V B.

endoergic channels up to and including complete atomization. The opening of these channels is evidenced by the rapid decrease in the measured merged-beams rate coefficient above the relevant threshold energies. To calculate the threshold energies for these competing reactions, we used literature values for the dissociation energies of H_3^+, H_2D^+, and D_2H^+ and all relevant diatomic molecules,[58,66] as well as the needed electron binding energies.[67]

For reaction (6), the competing channels are

$$D + H_3^+ \rightarrow HD + H_2^+ - 1.65\ \text{eV}, \tag{29a}$$

$$\rightarrow H_2 + HD^+ - 1.67\ \text{eV} \tag{29b}$$

$$\rightarrow HD + H + H^+ - 4.30\ \text{eV}, \tag{29c}$$

$$\rightarrow H_2 + [D + H]^+ - 4.34\ \text{eV}, \tag{29d}$$

$$\rightarrow HD^+ + H + H\ - 6.15\ \text{eV}, \tag{29e}$$

$$\rightarrow H_2^+ + D + H - 6.17\ \text{eV}, \tag{29f}$$

$$\rightarrow [D + H + H + H]^+ - 8.82\ \text{eV}. \tag{29g}$$

The square brackets indicate that the location of the final charge could be on any of the included atoms. Additional details have been given previously.[26] Similarly, for reactions (7) and (8), the competing reaction channels are

$$D + H_2D^+ \rightarrow D_2 + H_2^+ - 1.66\ \text{eV} \tag{30a}$$

$$\rightarrow HD + HD^+ - 1.68\ \text{eV} \tag{30b}$$

$$\rightarrow H_2 + D_2^+ - 1.70\ \text{eV} \tag{30c}$$

$$\rightarrow D_2 + H + H^+ - 4.31\ \text{eV} \tag{30d}$$

$$\rightarrow HD + [D + H]^+ - 4.35\ \text{eV} \tag{30e}$$

$$\rightarrow H_2 + D + D^+ - 4.39\ \text{eV} \tag{30f}$$

$$\rightarrow D_2^+ + H + H - 6.18\ \text{eV} \tag{30g}$$

$$\rightarrow HD^+ + D + H - 6.20\ \text{eV} \tag{30h}$$

$$\rightarrow H_2^+ + D + D - 6.21\ \text{eV} \tag{30i}$$

$$\rightarrow [D + D + H + H]^+ - 8.86\ \text{eV} \tag{30j}$$

and

$$D + D_2H^+ \rightarrow D_2 + HD^+ - 1.69\ \text{eV} \tag{31a}$$

$$\rightarrow HD + D_2^+ - 1.71\ \text{eV} \tag{31b}$$

$$\rightarrow D_2 + [D + H]^+ - 4.36\ \text{eV} \tag{31c}$$

$$\rightarrow HD + D + D^+ - 4.40\ \text{eV} \tag{31d}$$

$$\rightarrow D_2^+ + D + H - 6.23\ \text{eV} \tag{31e}$$

$$\rightarrow HD^+ + D + D - 6.25\ \text{eV} \tag{31f}$$

$$\rightarrow [D + D + D + H]^+ - 8.92\ \text{eV}. \tag{31g}$$

The thresholds appear to cluster around ~ 1.65 eV, ~ 4.35 eV, ~ 6.2 eV, and ~ 8.9 eV. They correspond, in energetic order and for all their isotopic variants, to the production of a pair of diatomics, the production of a neutral molecule and an atomic ion or a molecular ion and a neutral atom, and full atomization. These channels are aggregated into four distinct thresholds in the model described below.

C. Cross section model

A semiempirical model, initially developed for reaction (6) and introduced in our previous publication,[26] was slightly modified and applied to our experimental results for reactions (7) and (8). A brief overview of the model is provided here.

The model follows a Langevin-like formalism for scattering events with an energy barrier.[68] Our model also takes into account the internal excitation of the reactant molecular cations, as well as the opening of competing endoergic reaction channels. We adopt an impact parameter formulation of the cross section, assuming that the dynamics follows the IRC reaction coordinate s, which describes the relative motion of D and the triatomic cation up to the transition state,

$$\sigma_{ts}(E_r, E_{int}) = 2\pi \int_0^{b_{max}} P(b, E_{ts}) b db, \tag{32}$$

© Author(s) 2021

where E_{ts} is the total reaction energy available to overcome the barrier of the transition state at some impact parameter b and $P(b, E_{ts})$ is the corresponding probability. If we assume that the internal excitation energy, E_{int}, is available to combine with E_r to overcome any reaction barriers, we may write

$$E_{ts} = E_r + E_{int} - E_b - \frac{b^2 E_r}{R_b^2}, \tag{33}$$

where R_b is the radial separation of the centers-of-mass of the reactants, R_{cm}, at the transition state. The evolution of R_{cm} along the IRC coordinate s is shown in Fig. 8, together with that of individual interatomic distances. Reactions (6)–(8) may go forward, provided that the system overcomes the energy barrier E_b, i.e.,

$$P(b, E_{ts}) = H(E_{ts}), \tag{34}$$

where H is the Heaviside function. Simple integration yields the classical result,

$$\sigma_b(E_r, E_{int}) = \begin{cases} 0 & \text{for } E_r + E_{int} < E_b \\ \pi R_b^2 \left[1 + \frac{E_{int} - E_b}{E_r}\right] \times S(E_r, E_{int}) & \text{for } E_r + E_{int} \geq E_b, \end{cases} \tag{35}$$

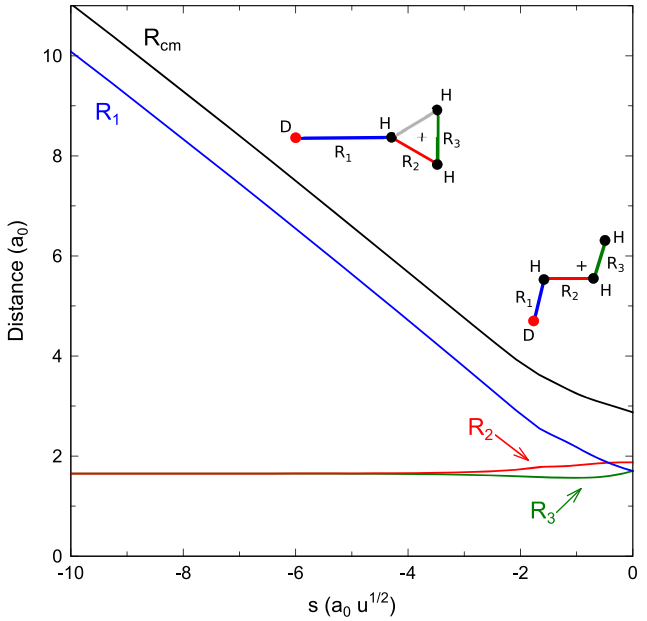

FIG. 8. Evolution of interatomic distances along the IRC coordinate s. R_{cm} is the distance between the D atom and the center-of-mass of the H_3^+ moiety (marked by the plus sign).

where we have introduced a flux reduction factor, $S(E_r, E_{int})$, to take into account the other competing channels. This factor is given in the following form:

$$S(E_r, E_{int}) = \begin{cases} 1 & E'_r < E_1 \\ \left[1 + a_1(E'_r - E_1)\right]^{-2} & E_1 \leq E'_r < E_2 \\ \left[1 + a_1(E'_r - E_1) + a_2(E'_r - E_2)^2\right]^{-2} & E_2 \leq E'_r < E_3 \\ \left[1 + a_1(E'_r - E_1) + a_2(E'_r - E_2)^2 + a_3(E'_r - E_3)^2\right]^{-2} & E_3 \leq E'_r < E_4 \\ \left[1 + a_1(E'_r - E_1) + a_2(E'_r - E_2)^2 + a_3(E'_r - E_3)^2 + a_4(E_r + E_{int} - E_4)^3\right]^{-2} & E'_r \geq E_4. \end{cases} \tag{36}$$

The threshold energies, E_k, are defined as the energy at which the successive competing reaction channels become accessible (see Sec. V B), E'_r is defined as $E'_r = E_r + fE_{int}$, and a_k and f are adjustable parameters, the latter representing the fraction of internal energy available to overcome the various thresholds. The thresholds have been grouped when nearly degenerate, e.g., reactions (29a) and (29b), reducing their number to 4. The choice of exponent is guided by the multiplicity of the breakup channels, being set to $n-1$ for n-body breakup. Note that f is set to unity for the atomization channel.

Within this potential scattering approach, the Langevin value, σ_L, is the upper limit for the cross section. From the above discussion of the differentreaction paths leading to deuterated products (Sec. IV A), our expression of the reaction cross section becomes

$$\sigma(E_r, E_{int}) = \frac{1}{N} \sum_i^{N_r} \min[\sigma_{b,i}(E_r, E_{int}), \sigma_L(E_r)], \tag{37}$$

where N is the total number of outgoing reaction paths and N_r is the number of reaction paths leading to deuteration. This formulation is needed to take into account the differing barrier height encountered in reaction (7) depending on whether H or D from H_2D^+ is pointing toward the colliding D atom.

Our model cross section, σ_{mod}, is generated by convolving Eq. (37) over E_{int}. The resulting expression is

© Author(s) 2021

$$\sigma_{\mathrm{mod}}(E_{\mathrm{r}},\langle E_{\mathrm{int}}\rangle) = \frac{1}{\langle E_{\mathrm{int}}\rangle}\int_0^\infty \sigma(E_{\mathrm{r}},E_{\mathrm{int}})\exp(-E_{\mathrm{int}}/\langle E_{\mathrm{int}}\rangle)dE_{\mathrm{int}}, \tag{38}$$

where $\langle E_{\mathrm{int}}\rangle$ is a function of the internal temperature T_{int} of the molecular cation and is derived from the partition function $Z(T)$,

$$\langle E_{\mathrm{int}}\rangle = k_{\mathrm{B}}T_{\mathrm{int}}^2\frac{1}{Z}\frac{\partial Z}{\partial T_{\mathrm{int}}}, \tag{39}$$

where k_{B} is the Boltzmann constant. Here, we apply the partition function of Kylänpää and Rantala[69] to H_3^+, that of Sidhu and Tennyson[70] to H_2D^+, and that of Ramanlal and Tennyson[56] to D_2H^+.

The model merged-beams rate coefficients are determined by multiplying σ_{mod} by v_{r} and by adjusting the parameters a_k, f, R_{b}, and $\langle E_{\mathrm{int}}\rangle$ to reproduce the measured rate coefficients. The resulting fits are plotted in Fig. 7. The values of the derived fit parameters listed in Table IV are quite similar to those extracted from our previous study of reaction (6).[26] The overall magnitude of σ_{mod} is mainly determined by the value of R_{b}. As mentioned above, our experimentally derived value of R_{b} can be compared to our theoretically derived value of $R_{\mathrm{cm}}(s = 0) = 2.873\ a_0$ shown in Fig. 8. The latter value is identical to 2.87 a_0 given by Hillenbrand *et al.*,[26] which was deduced from the geometries of Sanz-Sanz *et al.*[41] Taking into account the 15% systematic uncertainty in the absolute scale of our experimental data, R_{b} and $R_{\mathrm{cm}}(s = 0)$ are in reasonably good agreement. This is an important indication for the consistency of our analysis.

The parameter f appears to jump from a percent (albeit with a large error bar) to unity when going from reaction (6) to reactions (7) and (8). In the case of reaction (6), the low f value is indicative of a substantial internal excitation being transferred to the diatomic products of reactions (29a) and (29b). However, for all three reactions, it appears that there are an insufficient number of data points to reliably constrain f, making its evolution with deuteration somewhat inconclusive. The best fit values of $\langle E_{\mathrm{int}}\rangle$ for reactions (6)–(8) correspond to T_{int} = 1130 K, 1280 K, and 1200 K, respectively.

The various fragmentation channels competing with deuteration of the triatomic cation evolve in importance along the deuteration chain, as revealed by the decreasing value of a_1 and the concomitant increase in a_2, while a_3 and a_4 remain negligible throughout. Variable a_1 is a measure of the importance of the first endoergic threshold and corresponds to the formation of a neutral molecule and a molecular cation: reactions (29a)–(29b), (30a)–(30c), and (31a)–(31b). The variable a_2 is a measure of the importance of the second endoergic threshold and corresponds to the additional fragmentation of that cation: reactions (29c)–(29d), (30d)–(30f), and (31c)–(31d). It is tempting to attribute the predominance of multiple fragmentation for heavier systems to the increased residence time in the Min_2 potential well of the deuterated H_4^+. More insight could be gained with the help of advanced quantum dynamical methods such as MCTDH (Multi-configuration Time-Dependent Hartree Method).[71]

To incorporate the effect of quantum tunneling, the Heaviside function in Eq. (34) may be replaced by the energy dependent tunneling probability $\kappa(b, E_{\mathrm{ts}})$ evaluated with the help of the reaction energy profiles given in Sec. IV E,

$$\sigma_{\mathrm{tun}}(E_{\mathrm{r}},E_{\mathrm{int}}) = \left(2\pi\int_0^\infty \kappa(b,E_{\mathrm{ts}})bdb\right)S(E_{\mathrm{r}},E_{\mathrm{int}}), \tag{40}$$

with E_{ts} depending on b according to Eq. (33). Here, the tunneling correction is insignificant due to the high level of internal excitation in our experiments and does not improve the fit of the semiempirical model to the experimental results. It will, nevertheless, prove essential when deriving low temperature thermal rate coefficients, as discussed below.

D. Translational temperature and thermal rate coefficients

To be applicable to lower internal temperatures (T_{int} < 500 K), our model cross section, Eq. (38), needs to be adapted to the discrete character of the partition function,

$$\sigma_{\mathrm{disc}}(E_{\mathrm{r}},T_{\mathrm{int}}) = \frac{1}{Z}\sum_i \sigma(E_{\mathrm{r}},E_i)(2J_i+1)g_i\exp\left(-\frac{E_i}{k_{\mathrm{B}}T_{\mathrm{int}}}\right), \tag{41}$$

where E_i, J_i, and g_i are the energy, total angular momentum, and spin multiplicity of rovibrational state i of the triatomic reactant. The corresponding line lists were taken from the work of Mizus *et al.*[72] for H_3^+ and from the work of Sochi and Tennyson[73] for H_2D^+. In the case of D_2H^+, no such line list was available, so we have generated a low-energy line list from the most recent spectroscopic parameters[74] by means of the SPFIT/SPCAT package.[75] This discrete sum is replaced above $T \sim 800$ K by the integral over internal energy

TABLE IV. Best fit parameters for the model cross section and the flux reduction factor. Energetic thresholds are average values for reactions differing by isotopic substitution only. The uncertainties in the last one or two digits are given in parentheses.

Reactants	R_{b} (a_0)	$\langle E_{\mathrm{int}}\rangle$ (eV)	f	E_1 (eV)	a_1 (eV^{-1})	E_2 (eV)	a_2 (eV^{-2})	E_3 (eV)	a_3 (eV^{-2})	E_4 (eV)	a_4 (eV^{-3})
$D + H_3^+$	2.539(5)	0.183(2)	0.01(8)	1.66	0.296(4)	4.32	0.019(2)	6.16	0.001(6)	8.82	0.010(9)
	2.53[a]	0.185[a]	0.2[a]		0.3[a]						
$D + H_2D^+$	2.571(8)	0.222(2)	1.00(13)	1.68	0.223(6)	4.35	0.078(6)	6.20	0.001(27)	8.86	0.00(12)
$D + D_2H^+$	2.571(14)	0.201(4)	1.00(26)	1.70	0.199(8)	4.38	0.091(12)	6.24	0.00(3)	8.92	0.00(11)

[a]Reference 26.

© Author(s) 2021

E_{int}, as given by Eqs. (38) and (39). With this further refinement, a model thermal rate coefficient may computed as

$$k(T) = \left(\frac{8}{\pi\mu k_B^3 T^3}\right)^{1/2} \int_0^\infty \sigma(E_r, T_{int}) E_r \exp\left(-\frac{E_r}{k_B T}\right) dE_r. \quad (42)$$

Here, $\sigma(E_r, T_{int})$ is given by Eqs. (35), (37), and (41) for our model without tunneling and Eqs. (37), (40), and (41) for our model with tunneling. T refers to the translational temperature of the gas, T_{gas}. Setting $T_{int} = 0$ K yields a translational temperature rate coefficient. For thermal equilibrium between the translational and internal energy, $T_{gas} = T_{int}$. The resulting thermal rate coefficients for reactions (6)–(8) are given by the full and dashed curves in Fig. 9, depending on whether tunneling is incorporated (k_{tun}) or not (k_{mod}) in the evaluation of the reaction cross section. Their values are tabulated for all three systems in Tables SVIII–SX of the supplementary material. The values published before[26] for reaction (6) are superseded by these newer results where we have included the quantum tunneling probability in the model cross section and have performed a more careful thermal averaging.

In order to facilitate the implementation of our results into astrochemical models, we have fit the entire set of model thermal rate coefficients, both without and with the tunneling correction for the reaction cross section, with the commonly used Arrhenius–Kooij formula, giving

$$k_{arr}(T) = \alpha\left(\frac{T}{300\text{ K}}\right)^\beta \exp\left(-\frac{\gamma}{T}\right), \quad (43)$$

where α, β, and γ are fitting parameters. This fit is accurate to within 10% over the range $T = 10$ K–4000 K. The corresponding parameters are listed in Table V. For the classical over-the-barrier cross section model, we may interpret γ as the effective barrier height expressed in K. We find 64.7 meV, 70.7 meV, and 79.2 meV for reactions (6)–(8), respectively, somewhat below the values of E_b listed in Table II. Applying the common definition of the activation barrier[76] to Eq. (43),

$$E_a = k_B T^2 \frac{d \ln k(T)}{dT} = k_B(\gamma + \beta T), \quad (44)$$

we observe that E_a slowly grows with temperature, given the values of β and γ listed in Table V.

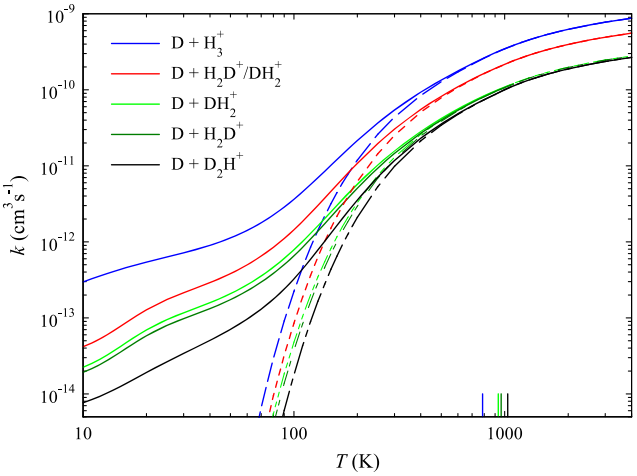

FIG. 9. Rate coefficient, k, vs temperature, T, for reactions (6)–(8). For reaction (7), the two paths are separated, as discussed in Sec. IV A. The full curves (k_{tun}) include the tunnel corrected cross section described in Sec. V C, while the dashed curves (k_{mod}) use the classical expression for the cross section given by Eq. (35). The energy of the barrier for each reaction, E_b/k_B, is indicated on the T axis by a vertical marker. The light green marker overlaps the red marker.

TABLE V. Parameters for the fits of the Arrhenius–Kooij formula (43) to the thermal rate coefficients derived from our model without and with tunneling. All fit functions describe our results with a relative accuracy of 10% or better across the given temperature range, $T_{min} \le T \le T_{max}$.

Reactants	Tunneling	α[a] (cm^3 s^{-1})	β	γ (K)	T_{min} (K)	T_{max} (K)
D + H$_3^+$	No	5.43[−10]	0.26	751	80	4000
	Yes	4.89[−12]	0.81	0	10	65
	Yes	5.26[−11]	2.37	0	65	257
	Yes	3.62[−10]	0.43	573	257	4000
D + H$_2$D$^+$	No	3.94[−10]	0.20	821	80	4000
	Yes	3.14[−12]	1.06	8	10	73
	Yes	3.10[−11]	2.75	0	73	210
	Yes	2.26[−10]	0.44	590	210	4000
D + D$_2$H$^+$	No	2.13[−10]	0.17	919	80	4000
	Yes	9.79[−13]	1.45	0	10	73
	Yes	1.24[−11]	3.25	0	73	206
	Yes	1.19[−10]	0.41	686	206	4000

[a] $X[Y]$ corresponds to $X \times 10^Y$.

E. Comparison to theory

As we have reevaluated the thermal rate coefficient for reaction (6) and extended our model to reaction (7), we may compare our classical over-the-barrier thermal results with the predictions of Bulut *et al.*[59] obtained with the Ring Polymer Molecular Dynamics (RPMD) approach for these two reactions. Such a comparison is given in Fig. 10, together with the pure translational rate coefficients obtained by setting $T_{int} = 0$ in the evaluation of the cross section. The RPMD rate coefficient lies below our modeled thermal results but close to the pure translational case. Bulut *et al.* attributed the difference between the RPMD results and experimental values to the possible existence of non-thermal vibrational excitation of H_3^+ in our original model.[59] The now explicit treatment of internal excitation embodied in Eq. (41) should prevent such spurious excitations from affecting our modeled rate coefficient. Hence, it is unclear why the RPMD results lie below our thermal model results. A partial explanation may be that there are a large number of trapped trajectories in the RPMD calculations that form long-lived complexes with lifetimes longer than the 1 ns simulated in the calculations. RPMD is also expected to incorporate tunneling, but no obvious enhancement of the rate coefficient is visible at the lower end of the temperature range studied. We expect that some unknown fraction of the trapped trajectories will contribute to tunneling. It is clear that additional

© Author(s) 2021

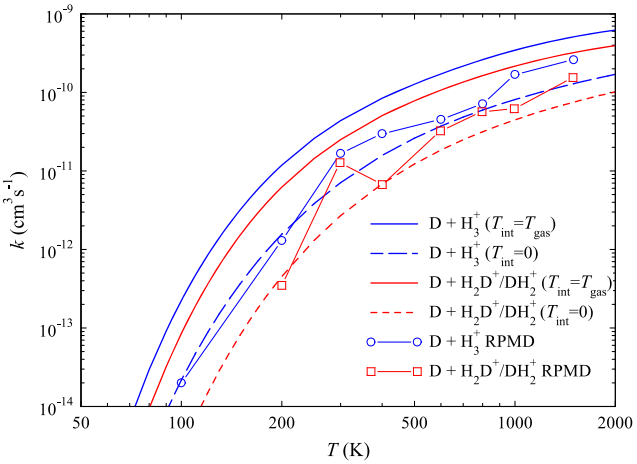

FIG. 10. Rate coefficient, k, vs temperature, T for reactions (6) and (7). The full curves are computed with $T_{int} = T_{gas}$, while the dashed curves are computed by setting $T_{int} = 0$. The symbols are the RPMD calculations of Bulut *et al.*[59]

theoretical and experimental work is called for in order to better understand these reactions.

VI. SUMMARY

We have reported here a combined experimental and theoretical study of atomic D reacting with H_3^+, H_2D^+, and D_2H^+, leading to the formation of H_2D^+, D_2H^+, and D_3^+, respectively. A high-level calculation of the vibrationally adiabatic minimum energy path, combined with an extended version of our classical over-the-barrier model, produces an excellent fit to our measured merged-beams rate coefficients. The rate coefficient is found to scale with the number of available sites for deuteration. The proper evaluation of the tunneling probability, together with the inclusion of individual rovibrational levels, allows us to extend the calculation of thermal rate coefficients based on our model down to 10 K. Our results do not agree with those of Bulut *et al.* obtained with the RPMD approach.[59]

SUPPLEMENTARY MATERIAL

See the supplementary material for a tabulation of the curves shown in Fig. 3 (Tables SI–SV), Fig. 7 (Tables SVI–SVII), and Fig. 9 (Tables SVIII–SX).

ACKNOWLEDGMENTS

The authors thank Octavio Roncero for stimulating conversations and Anthony Roucou for having computed the level list for D_2H^+. This research was supported, in part, by the NSF Division of Astronomical Sciences Astronomy and Astrophysics Grants program under AST-1613267 and AST-2002461. P.-M.H. was supported, in part, by the German Research Foundation (DFG) under Grant No. HI 2009/1-1. J.L. thanks the ULB/VUB computing center and the Consortium des Equipements de Calcul Intensif (Fonds de la Recherche Scientifique-FNRS and Walloon Region) for computational support. X.U. is a Senior Research Associate of the Fonds de la Recherche Scientifique-FNRS and acknowledges travel support from the Fonds de la Recherche Scientifique-FNRS through IISN (Grant No. 4.4504.10). Part of this work was made possible because of the DYMCOM workshop, fully supported by the Institut Pascal (Université Paris-Saclay).

DATA AVAILABILITY

The data that support the findings of this study are available within the article and its supplementary material.

REFERENCES

[1] J. Meyer and R. Wester, Annu. Rev. Phys. Chem. **68**, 333 (2017).
[2] D. McElroy, C. Walsh, A. J. Markwick, M. A. Cordiner, K. Smith, and T. J. Millar, Astron. Astrophys. **550**, A36 (2013).
[3] V. Wakelam, J.-C. Loison, E. Herbst, B. Pavone, A. Bergeat, K. Béroff, M. Chabot, A. Faure, D. Galli, W. D. Geppert, D. Gerlich, P. Gratier, N. Harada, K. M. Hickson, P. Honvault, S. J. Klippenstein, S. D. L. Picard, G. Nyman, M. Ruaud, S. Schlemmer, I. R. Sims, D. Talbi, J. Tennyson, and R. Wester, Astrophys. J. Suppl. Ser. **217**, 20 (2015).
[4] J. Prager, U. Riedel, and J. Warnatz, Proc. Combust. Inst. **31**, 1129 (2007).
[5] D. Kim, F. Rizzi, K. W. Cheng, J. Han, F. Bisetti, and O. M. Knio, Combust. Flame **162**, 2904 (2015).
[6] J. G. Wang and P. C. Stancil, Phys. Scr. **T96**, 72 (2002).
[7] Y. H. Kim, J. L. Fox, J. H. Black, and J. I. Moses, J. Geophys. Res. **119**, 384, https://doi.org/10.1002/2013ja019022 (2014).
[8] V. Vuitton, O. Dutuit, M. A. Smith, and N. Balucani, in *Titan: Interior, Surface, Atmosphere, and Space Environment*, edited by I. Müller-Wodarg, C. A. Griffith, E. Lellouch, and T. E. Cravens (Cambridge University Press, Cambridge, UK, 2014), pp. 224–284.
[9] N. S. Shuman, D. E. Hunton, and A. A. Viggiano, Chem. Rev. **115**, 4542 (2015).
[10] K. Hassouni, F. Silva, and A. Gicquel, J. Phys. D **43**, 153001 (2010).
[11] Y. Sakiyama, D. B. Graves, H.-W. Chang, T. Shimizu, and G. E. Morfill, J. Phys. D **45**, 425201 (2012).
[12] V. G. Anicich, J. Phys. Chem. Ref. Data **22**, 1469 (1993).
[13] T. Sahoo, S. Ghosh, S. Adhikari, R. Sharma, and A. J. C. Varandas, J. Chem. Phys. **142**, 024304 (2015).
[14] M. Lara, P. G. Jambrina, F. J. Aoiz, and J.-M. Launay, J. Chem. Phys. **143**, 204305 (2015).
[15] C. Sanz-Sanz, A. Aguado, O. Roncero, and F. Naumkin, J. Chem. Phys. **143**, 234303 (2015).
[16] F. Meng, T. Wang, and D. Wang, J. Chem. Phys. **135**, 114307 (2011).
[17] H. Bruhns, H. Kreckel, K. Miller, M. Lestinsky, B. Seredyuk, W. Mitthumsiri, B. L. Schmitt, M. Schnell, X. Urbain, M. L. Rappaport, C. C. Havener, and D. W. Savin, Rev. Sci. Instrum. **81**, 013112 (2010).
[18] P. G. Jambrina, J. M. Alvariño, D. Gerlich, M. Hankel, V. J. Herrero, V. Sáez-Rábanos, and F. J. Aoiz, Phys. Chem. Chem. Phys. **14**, 3346 (2012).
[19] S. C. Althorpe and D. C. Clary, Annu. Rev. Phys. Chem. **54**, 493 (2003).
[20] J. M. Bowman, G. Czakó, and B. Fu, Phys. Chem. Chem. Phys. **13**, 8094 (2011).
[21] T. González-Lezana and P. Honvault, Int. Rev. Phys. Chem. **33**, 371 (2014).
[22] P. Allmendinger, J. Deiglmayr, O. Schullian, K. Höveler, J. A. Agner, H. Schmutz, and F. Merkt, Chem. Phys. Chem. **17**, 3596 (2016).
[23] E. Hugo, O. Asvany, and S. Schlemmer, J. Chem. Phys. **130**, 164302 (2009).
[24] K. N. Crabtree, C. A. Kauffman, B. A. Tom, E. Beçka, B. A. McGuire, and B. J. McCall, J. Chem. Phys. **134**, 194311 (2011).
[25] F. Grussie, M. H. Berg, K. N. Crabtree, S. Gärtner, B. J. McCall, S. Schlemmer, A. Wolf, and H. Kreckel, Astrophys. J. **759**, 21 (2012).
[26] P.-M. Hillenbrand, K. P. Bowen, J. Liévin, X. Urbain, and D. W. Savin, Astrophys. J. **877**, 38 (2019).

© Author(s) 2021

[27]A. P. O'Connor, X. Urbain, J. Stützel, K. A. Miller, N. de Ruette, M. Garrido, and D. W. Savin, Astrophys. J. Suppl. Ser. **219**, 6 (2015).
[28]N. de Ruette, K. A. Miller, A. P. O'Connor, X. Urbain, C. F. Buzard, S. Vissapragada, and D. W. Savin, Astrophys. J. **816**, 31 (2015).
[29]P.-M. Hillenbrand, K. P. Bowen, F. Dayou, K. A. Miller, N. de Ruette, X. Urbain, and D. W. Savin, Phys. Chem. Chem. Phys. **22**, 27364 (2020).
[30]J. C. Rienstra-Kiracofe, G. S. Tschumper, H. F. Schaefer, S. Nandi, and G. B. Ellison, Chem. Rev. **102**, 231 (2002).
[31]A. P. O'Connor, F. Grussie, H. Bruhns, N. de Ruette, T. P. Koenning, K. A. Miller, D. W. Savin, J. Stützel, X. Urbain, and H. Kreckel, Rev. Sci. Instrum. **86**, 113306 (2015).
[32]R. Bruckmeier, C. Wunderlich, and H. Figger, Phys. Rev. Lett. **72**, 2550 (1994).
[33]U. Galster, F. Baumgartner, U. Müller, H. Helm, and M. Jungen, Phys. Rev. A **72**, 062506 (2005).
[34]D. G. Seely, H. Bruhns, D. W. Savin, T. J. Kvale, E. Galutschek, H. Aliabadi, and C. C. Havener, Nucl. Instrum. Methods A **585**, 69 (2008).
[35]D. H. Crandall, J. A. Ray, and C. Cisneros, Rev. Sci. Instrum. **46**, 562 (1975).
[36]D. W. Savin, L. D. Gardner, D. B. Reisenfeld, A. R. Young, and J. L. Kohl, Rev. Sci. Instrum. **66**, 67 (1995).
[37]F. Brouillard and W. Claeys, in *Physics of Ion-Ion and Electron-Ion Collisions*, edited by F. Brouillard and J. W. McGowan (Plenum Press, New York, 1983), pp. 415–459.
[38]H. Bruhns, H. Kreckel, K. A. Miller, X. Urbain, and D. W. Savin, Phys. Rev. A **82**, 042708 (2010).
[39]G. E. Moyano, D. Pearson, and M. A. Collins, J. Chem. Phys. **121**, 12396 (2004).
[40]A. Alijah and A. J. C. Varandas, J. Chem. Phys. **129**, 034303 (2008).
[41]C. Sanz-Sanz, O. Roncero, M. Paniagua, and A. Aguado, J. Chem. Phys. **139**, 184302 (2013).
[42]H.-J. Werner, P. J. Knowles, G. Knizia, F. R. Manby, and M. Schütz, Wiley Interdiscip. Rev.: Comput. Mol. Sci. **2**, 242 (2012).
[43]H.-J. Werner, P. J. Knowles, G. Knizia, F. R. Manby, M. Schütz *et al.*, "Molpro, version 2019.2, a package of *ab initio* programs" (2019), see https://www.molpro.net.
[44]P. J. Knowles and H.-J. Werner, Chem. Phys. Lett. **145**, 514 (1988).
[45]H.-J. Werner and P. J. Knowles, J. Chem. Phys. **89**, 5803 (1988).
[46]T. H. Dunning, Jr., J. Chem. Phys. **90**, 1007 (1989).
[47]R. A. Kendall, T. H. Dunning, and R. J. Harrison, J. Chem. Phys. **96**, 6796 (1992).
[48]M. J. Frisch, G. W. Trucks, H. B. Schlegel, G. E. Scuseria, M. A. Robb, J. R. Cheeseman, G. Scalmani, V. Barone, G. A. Petersson, H. Nakatsuji, X. Li, M. Caricato, A. V. Marenich, J. Bloino, B. G. Janesko, R. Gomperts, B. Mennucci, H. P. Hratchian, J. V. Ortiz, A. F. Izmaylov, J. L. Sonnenberg, D. Williams-Young, F. Ding, F. Lipparini, F. Egidi, J. Goings, B. Peng, A. Petrone, T. Henderson, D. Ranasinghe, V. G. Zakrzewski, J. Gao, N. Rega, G. Zheng, W. Liang, M. Hada, M. Ehara, K. Toyota, R. Fukuda, J. Hasegawa, M. Ishida, T. Nakajima, Y. Honda, O. Kitao, H. Nakai, T. Vreven, K. Throssell, J. A. Montgomery, Jr., J. E. Peralta, F. Ogliaro, M. J. Bearpark, J. J. Heyd, E. N. Brothers, K. N. Kudin, V. N. Staroverov, T. A. Keith, R. Kobayashi, J. Normand, K. Raghavachari, A. P. Rendell, J. C. Burant, S. S. Iyengar, J. Tomasi, M. Cossi, J. M. Millam, M. Klene, C. Adamo, R. Cammi, J. W. Ochterski, R. L. Martin, K. Morokuma, O. Farkas, J. B. Foresman, and D. J. Fox, Gaussian 16 Revision C.01 (Gaussian, Inc., Wallingford, CT, 2016).
[49]C. Gonzalez and H. B. Schlegel, J. Chem. Phys. **90**, 2154 (1989).
[50]C. Gonzalez and H. B. Schlegel, J. Phys. Chem. **94**, 5523 (1990).
[51]K. Fukui, J. Phys. Chem. **74**, 4161 (1970).
[52]W. H. Miller, N. C. Handy, and J. E. Adams, J. Chem. Phys. **72**, 99 (1980).
[53]B. C. Garrett, M. J. Redmon, R. Steckler, D. G. Truhlar, K. K. Baldridge, D. Bartol, M. W. Schmidt, and M. S. Gordon, J. Phys. Chem. **92**, 1476 (1988).
[54]A. G. Baboul and H. B. Schlegel, J. Chem. Phys. **107**, 9413 (1997).
[55]J. A. Pople, M. Head-Gordon, and K. Raghavachari, J. Chem. Phys. **87**, 5968 (1987).
[56]J. Ramanlal and J. Tennyson, Mon. Not. R. Astron. Soc. **354**, 161 (2004).
[57]C. P. Morong, J. L. Gottfried, and T. Oka, J. Mol. Spec. **255**, 13 (2009).
[58]R. Jaquet, Mol. Phys. **111**, 2606 (2013).
[59]N. Bulut, A. Aguado, C. Sanz-Sanz, and O. Roncero, J. Phys. Chem. A **123**, 8766 (2019).
[60]C. Eckart, Phys. Rev. **35**, 1303 (1930).
[61]H. S. Johnston and J. Heicklen, J. Phys. Chem. **66**, 532 (1962).
[62]R. A. Marcus, J. Chem. Phys. **46**, 959 (1967).
[63]Y. Wang and J. M. Bowman, J. Chem. Phys. **129**, 121103 (2008).
[64]R. J. Le Roy, K. A. Quickert, and D. J. Le Roy, Trans. Faraday Soc. **66**, 2997 (1970).
[65]Y. Georgievskii and S. J. Klippenstein, J. Phys. Chem. A **111**, 3802 (2007).
[66]K. Huber and G. Herzberg, *Molecular Spectra and Molecular Structure: Constants of Diatomic Molecules*, Vol. IV (Springer US, 1979).
[67]A. Kramida, Y. Ralchenko, J. Reader, and NIST ASD Team, *NIST Atomic Spectra Database* (version 5.5.6) [online] (NIST, 2018).
[68]R. D. Levine, *Molecular Reaction Dynamics* (Cambridge University Press, Cambridge, 2005).
[69]I. Kylänpää and T. T. Rantala, J. Chem. Phys. **135**, 104310 (2011).
[70]K. Sidhu, S. Miller, and J. Tennyson, Astron. Astrophys. **255**, 453 (1992).
[71]H.-D. Meyer, U. Manthe, and L. S. Cederbaum, Chem. Phys. Lett. **165**, 73 (1990).
[72]I. I. Mizus, A. Alijah, N. F. Zobov, L. Lodi, A. A. Kyuberis, S. N. Yurchenko, J. Tennyson, and O. L. Polyansky, Mon. Not. R. Astron. Soc. **468**, 1717 (2017).
[73]T. Sochi and J. Tennyson, Mon. Not. R. Astron. Soc. **405**, 2345 (2010).
[74]C. R. Markus, P. A. Kocheril, and B. J. McCall, J. Mol. Spectrosc. **355**, 8 (2019).
[75]H. M. Pickett, J. Mol. Spectrosc. **148**, 371 (1991).
[76]K. J. Laidler, J. Chem. Education **61**, 494 (1984).

© Author(s) 2021